

# Search for VHE gamma rays from SS433/W50 with the CANGAROO-II telescope

Sei. Hayashi<sup>a,1</sup>, F. Kajino<sup>a</sup>, T. Naito<sup>b</sup>, A. Asahara<sup>c</sup>, G.V. Bicknell<sup>d</sup>, R.W. Clay<sup>e</sup>, Y. Doi<sup>f</sup>, P.G. Edwards<sup>g</sup>, R. Enomoto<sup>h</sup>, S. Gunji<sup>f</sup>, S. Hara<sup>i</sup>, T. Hara<sup>b</sup>, T. Hattori<sup>j</sup>, C. Itoh<sup>i</sup>, S. Kabuki<sup>c</sup>, H. Katagiri<sup>k</sup>, A. Kawachi<sup>j</sup>, T. Kifune<sup>h</sup>, L.T. Ksenofontov<sup>h</sup>, H. Kubo<sup>c</sup>, T. Kurihara<sup>j</sup>, R. Kurosaka<sup>h</sup>, J. Kushida<sup>j</sup>, Y. Matsubara<sup>l</sup>, Y. Miyashita<sup>j</sup>, Y. Mizumoto<sup>m</sup>, M. Mori<sup>h</sup>, H. Moroi<sup>j</sup>, H. Muraishi<sup>n</sup>, Y. Muraki<sup>a</sup>, T. Nakase<sup>j</sup>, D. Nishida<sup>c</sup>, K. Nishijima<sup>j</sup>, M. Ohishi<sup>h</sup>, K. Okumura<sup>h</sup>, J.R. Patterson<sup>e</sup>, R.J. Protheroe<sup>e</sup>, N. Sakamoto<sup>f</sup>, K. Sakurazawa<sup>o</sup>, D.L. Swaby<sup>e</sup>, T. Tanimori<sup>c</sup>, H. Tanimura<sup>c</sup>, G. Thornton<sup>e</sup>, F. Tokana<sup>i</sup>, K. Tsuchiya<sup>p</sup>, T. Uchida<sup>h</sup>, S. Watanabe<sup>c</sup>, T. Yamaoka<sup>a</sup>, S. Yanagita<sup>q</sup>, T. Yoshida<sup>q</sup>, T. Yoshikoshi<sup>h</sup>

<sup>a</sup>Department of Physics, Konan University, Kobe, Hyogo 658-8501, Japan

<sup>b</sup>Faculty of Management Information, Yamanashi Gakuin University, Kofu, Yamanashi 400-8575, Japan

<sup>c</sup>Department of Physics, Graduate School of Science, Kyoto University, Sakyo-ku, Kyoto 606-8502, Japan

<sup>d</sup>Research School of Astronomy and Astrophysics, Australian National University, ACT 2611, Australia

<sup>e</sup>School of Chemistry and Physics, University of Adelaide, SA 5005, Australia

<sup>f</sup>Department of Physics, Yamagata University, Yamagata, Yamagata 990-8560, Japan

<sup>g</sup>Paul Wild Observatory, CSIRO Australia Telescope National Facility, Narrabri, NSW 2390, Australia

<sup>h</sup>Institute for Cosmic Ray Research, University of Tokyo, Kashiwa, Chiba 277-8582, Japan

<sup>i</sup>Ibaraki Prefectural University of Health Sciences, Ami, Ibaraki 300-0394, Japan

<sup>j</sup>Department of Physics, Tokai University, Hiratsuka, Kanagawa 259-1292, Japan

<sup>k</sup>Department of Physical Science, Hiroshima University, Higashi-Hiroshima, Hiroshima 739-8526, Japan

<sup>l</sup>Solar-Terrestrial Environment Laboratory, Nagoya University, Nagoya, Aichi 464-8602, Japan

<sup>m</sup>National Astronomical Observatory of Japan, Mitaka, Tokyo 181-8588, Japan

<sup>n</sup>School of Allied Health Sciences, Kitasato University, Sagami-hara, Kanagawa 228-8555, Japan

<sup>o</sup>Department of Physics, Tokyo Institute of Technology, Meguro, Tokyo 152-8551, Japan

<sup>p</sup>National Research Institute of Police Science, Kashiwa, Chiba 277-0882, Japan

<sup>q</sup>Faculty of Science, Ibaraki University, Mito, Ibaraki 310-8512, Japan

## Abstract

SS433, located at the center of the supernova remnant W50, is a close proximity binary system consisting of a compact star and a normal star. Jets of material are directed outwards from the vicinity of the compact star symmetrically to the east and west. Non-thermal hard X-ray emission is detected from lobes lying on both sides. Shock accelerated electrons are expected to generate VHE gamma rays through the inverse-Compton process in the lobes. Observations of the western X-ray lobe region of SS433/W50 system have been performed to detect VHE gamma rays using the 10 m CANGAROO-II telescope in August and September, 2001, and July and September, 2002. The total observation times are 85.2 h for ON source, and 80.8 h for OFF source data. No significant excess of VHE gamma rays has been found at three regions of the western X-ray lobe of SS433/W50 system. We have derived 99% confidence level upper limits to the fluxes of gamma rays and have set constraints on the strengths of the magnetic fields assuming the synchrotron/inverse-Compton model for the wide energy range of photon spectrum from radio to TeV. The derived lower limits are 4.3  $\mu$ G for the center of the brightest X-ray emission region and 6.3  $\mu$ G for the far end from SS433 in the western X-ray lobe. In addition, we suggest that the spot-like X-ray emission may provide a major contribution to the hardest X-ray spectrum in the lobe.

**Key words:** gamma rays: observations, ISM: individual (W50), jets, stars: individual (SS433)

**PACS:** 95.85.Pw, 98.38.-j

## 1. Introduction

The galactic SNR W50 is a strong non-thermal radio source. Radio images of W50 show a structure extended over  $\sim 2^\circ \times 1^\circ$  with limb-brightened “ears” at the eastern and western ends [1, 2, 3, 4]. The radio emission from W50 peaks at 419 mJy at 4.75 GHz, with the spectral index varying from  $\alpha = 0.3$  to 1.0 (where  $S \propto \nu^{-\alpha}$ ) over the source in the frequency range 0.41–4.75 GHz [1]. The distance to W50 is estimated to be 5.5 kpc [5, 6], and the age is assumed to be about  $10^4$  years. SS433, located at R.A. (J2000) =  $19^h 11^m 49^s$ , Dec. (J2000) =  $+04^\circ 58' 48''$

is the jet source located at the center of W50 with a V-band optical magnitude of 14.2 [7]. SS433 is a close proximity binary system with an orbital period 13.1 days, consisting of a compact star and a normal star. Jets of material are directed symmetrically outwards from the vicinity of the compact star to east and west at a speed of about  $0.26c$  [8]. The axis of the jets is precessing in a cone with half-angle of  $20^\circ$ . The precession period is  $\sim 163$  days, and the system is oriented at an angle of  $\sim 79^\circ$  to the line of sight [8]. The compact star is not yet identified whether it is a black hole or neutron star. An evaluation is suggested by Hillwig et al. (2004) [9] that the system consists of a low-mass black hole with a mass of  $2.9 \pm 0.7 M_\odot$  and a type

*Email address:* shayashi@hep.konan-u.ac.jp (Sei. Hayashi)

A3–7 I supergiant with a mass of  $10.9 \pm 3.1 M_{\odot}$ .

Bright diffuse X-ray lobes on the eastern and western sides of SS433 were discovered by the *Einstein* observatory in 1983 [10], and were confirmed by *ROSAT* and *ASCA* measurements in 1997 [11]. These X-ray lobes are believed to have been formed by the jets emitted from SS433, as they are symmetrical about SS433 and lie along the same axis as that defined by the east-west elongation of the W50 radio shell and are within the precession cone of the SS433 jets. Initial *ROSAT* and *ASCA* measurements of the spectra of these X-ray lobes were compatible with both power-law model and thermal models [11]. Subsequently, however, the *ASCA* team reported harder power-law spectra of the western X-ray lobe in 2000. The spectra were found to become softer with distance from SS433 within the range of the photon index from  $\Gamma = 1.38$  to 2.39 [12, 13]. They also reported that the thermal model is acceptable only when an unusually low metal abundance is assumed. This indicated that the X-ray emissions of the western X-ray lobe have a non-thermal origin. These results were consistent with the picture that the high energy electrons are generated at the sides of the X-ray lobes closest to SS433, with the electrons losing their energy by the synchrotron emission as they travel further from SS433. The *ASCA* results suggest that very high energy electrons with energies up to several hundred TeV are expected to be produced through shock acceleration in the X-ray lobes, and the VHE gamma ray emissions are expected to be generated through the inverse-Compton (IC) scattering.

In 2005, the HEGRA team gave the flux upper limits on the VHE gamma rays at a few percent of the Crab nebula flux for the regions reported by the *ROSAT* and *ASCA* team in 1997 [14]. In an effort to detect VHE gamma rays, we observed the western X-ray lobe region with the CANGAROO-II air Cherenkov imaging telescope in 2001 and 2002, based on the *ASCA* result of 2000. We report the results of our observations and discuss the possible environmental conditions of the western X-ray lobe region.

## 2. Observations

The 10 m CANGAROO-II telescope [15] is located near Woomera, South Australia ( $136^{\circ}47'E$ ,  $31^{\circ}06'S$ , 160 m a.s.l.) and consists of 114 segmented spherical mirrors each of 80 cm diameter [16]. An imaging camera consisting of 552 PMTs is placed at the focal plane covering a field-of-view (FOV) of  $2^{\circ}76 \times 2^{\circ}76$ . The CANGAROO-II telescope has an angular resolution of  $0^{\circ}30$  (29 pc at a distance of 5.5 kpc) with an energy threshold of 850 GeV for a Crab-like energy spectrum.

The *ASCA* team reported the results of three regions in the western X-ray lobe in 2000, based on their high spatial and spectral resolving power over a wide energy range [12, 13]. These regions were named positions 1, 2 and 3 by the *ASCA* team in order of distance from SS433, centered  $23'$ ,  $31'$  and  $39'$  west of SS433, respectively. Hereafter, we call these regions “*p1*”, “*p2*” and “*p3*”, respectively (Fig. 1). According to the *ASCA* results, the region “*p1*” shows the hardest X-ray spectrum of the three regions and has a harder X-ray spectrum than the region “*w1*” which the *ROSAT* and *ASCA* team reported on

previously. The region “*p2*” includes the center of the brightest X-ray region and “*p3*” is the edge of the brightest region. The latter two regions have harder X-ray spectra than “*w2*”.

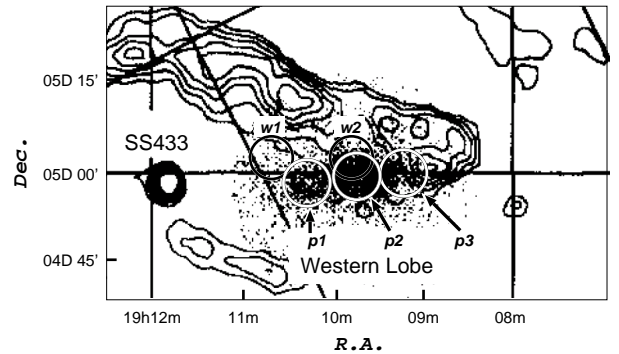


Figure 1: 4.75 GHz radio contour map of W50 overlaid on X-ray images of the western X-ray lobe (dots) obtained by *ASCA* [12]. Solid white circles show the regions reported by the *ASCA* team in 2000. In this paper, we label these regions “*p1*”, “*p2*” and “*p3*”. Solid black circles show the regions reported by the *ROSAT* and *ASCA* team in 1997, which are labeled “*w1*” and “*w2*”.

Observations of the western X-ray lobe region were performed using the CANGAROO-II telescope in August and September 2001, and in July and September 2002. Based on the *ASCA* results, the tracking position was set at “*p1*”, since the region showed the hardest power-law spectrum with the photon index of  $\Gamma = 1.38$ , suggesting shock acceleration could be taking place. The data were obtained by ON source observations tracking the source position, and by OFF source observations for the background. ON source observations were timed to contain the meridian passage of the target, as was done by Enomoto et al. [17]. Thus, the maximum elevation angle during the observations was about 54 degrees. OFF source observations were timed to have suitable offset right ascensions which varied day by day from  $-1^h36^m48^s$  to  $+4^h48^m18^s$ . The total observation times in 2001 were 51.4 h (ON source) and 49.5 h (OFF source) and, in 2002, 33.8 h (ON source) and 31.3 h (OFF source).

## 3. Analysis

We performed a preselection for the data analysis to obtain the data under good weather conditions. To reduce night-sky background noise, we selected air shower events having at least 4 adjacent pixels with more than  $\sim 3.3$  photoelectrons, which resulted in a stable shower rate. Periods of data with a shower rate less than 1.5 Hz were not used for the present analysis to eliminate the effects of partial cloud and dew formation on the mirrors. Moreover, in order to stabilize the shower rate, data taken at elevation angles less than  $40^{\circ}$  were not used. After these selections, 60.6% of the total observation time was used for the analysis (Table 1). The resulting mean elevation angle was approximately  $51^{\circ}$ .

To reduce the effects of the night-sky background, we have used the timing information. The pixels which were triggered more than  $30 \text{ nsec}$  from the average trigger time of a shower were eliminated. For each pixel, trigger counts within a  $700 \mu\text{s}$

Table 1: Observation time,  $t_{\text{obs}}$  hours, and selected time,  $t_{\text{sel}}$  hours, in 2001 and 2002.

Year	ON		OFF	
	$t_{\text{sel}}$	$t_{\text{obs}}$	$t_{\text{sel}}$	$t_{\text{obs}}$
2001	36.3	51.4	30.4	49.5
2002	17.2	33.8	16.7	31.3
Total	53.5	85.2	47.1	80.8

period were recorded once a second, and were checked during the off-line analysis to exclude pixels having high trigger rates, which were generally caused by the passage of a bright star through the FOV. Trigger counts were summed run by run to search for the effect of stars passing through the FOV. After excluding pixels having more the 15 triggers per  $700 \mu\text{s}$  period, there were no apparent effects of stars during the whole period of observations, including the brightest star with the magnitude of 4.9 in the OFF source observations on September 6 and 7 in 2002. Further, in each set of the data, we also eliminated a small number of pixels which showed deformed ADC spectra. The deformed ADC spectra were determined by the following procedure.

1. The ADC spectrum of each pixel was made for both years using the data which satisfied the trigger condition.
2. The averaged ADC spectrum of 48 reference pixels which were located at symmetrical positions in the focal plane with respect to the pixel being examined was defined as a reference for each pixel.
3.  $\chi^2$  of the ADC spectrum against the corresponding reference ADC spectrum was obtained as  $\chi^2_{\text{ADC}}$  for each pixel. In addition, the number of events which satisfied the trigger condition was compared with averaged number for the reference pixels, and the  $\chi^2$  of this number was obtained as  $\chi^2_{\text{entry}}$  for each pixel, too.
4. Pixels which had larger values of  $\chi^2_{\text{ADC}}$  and  $\chi^2_{\text{entry}}$  than selected threshold values were eliminated in order to obtain good shower images, since these were possibly due to a hardware fault.

After performing this procedure, the pixels having the deformed ADC spectra or high trigger rates were eliminated from the data of both years. For each shower event, the lower energy events which have smaller size shower images tend to be deformed by the hardware noise. To avoid this effect, we selected the events above the threshold SUMADC value (sum of ADC values of triggered pixels) of 2100 which corresponds to about 23 photoelectrons.

The analysis of the data was performed based on the imaging atmospheric Cherenkov technique [18, 19]. We calculated the imaging parameters (Hillas parameters), *Distance*, *Length*, *Width* using Monte Carlo (MC) simulations for gamma rays and OFF source data for cosmic rays. We selected the events under the conditions: the distance of the centroid of the image from the center of the FOV was less than  $1.3^\circ$  to eliminate the edge effect of the FOV of the camera, and  $0.2^\circ < \textit{Distance} < 1.2^\circ$ ,

to increase the accuracy of the orientation angle of the image, *Alpha* [20, 21]. To differentiate gamma ray like events from cosmic ray like events, we adopted the Likelihood method [22] which has a higher selection efficiency for gamma rays than a conventional parameterization technique. Figure 2 shows the MC results for the distributions of *Width* and *Length* of gamma rays, assuming a spectral index of  $-2.5$ . The observed points for cosmic rays (background) are shown by the dots in the same figure. The Likelihood method uses a single param-

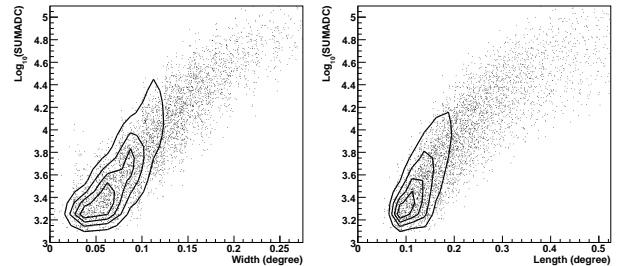


Figure 2: Distributions of *Width* (left panel) and *Length* (right panel) for gamma ray MC data (contours) and OFF-source experimental data (dots) in the energy range 0.2–50 TeV. Each parameter depends on SUMADC which is the sum of ADC values event by event, and is approximately proportional to the energy of the incident particle.

eter:  $L_{\text{ratio}} = P_{\gamma} / (P_{\gamma} + P_{\text{CR}})$ , where  $P_{\gamma}$  and  $P_{\text{CR}}$  are the probability of the event being due to a gamma ray and a cosmic ray, respectively. Both probabilities can be estimated from the products of individual probabilities for *Width* and *Length* which are derived from the probability density functions (PDFs), including its energy dependence. The PDFs were obtained using the MC for gamma ray initiated showers and the OFF source data for cosmic rays. Figure 3 shows the distributions of  $L_{\text{ratio}}$  expected for gamma rays and cosmic rays. In the region with  $L_{\text{ratio}} \leq 0.35$ , cosmic rays exceed gamma rays, whereas in the region with  $L_{\text{ratio}} \geq 0.35$ , gamma rays exceed cosmic rays. In this analysis, we used the data with  $L_{\text{ratio}} > 0.4$  to select the candidates of gamma rays. The subsequent selection of events with  $\textit{Alpha} \leq 20^\circ$  eliminates  $\sim 90\%$  of the cosmic ray events but retains  $\sim 60\%$  of the gamma ray events.

To check the feasibility of our observations and the analysis procedure, we analyzed Crab nebula data obtained in December 2000 using the same analysis code. Total analyzed times for ON source and OFF source data were 14.9 h and 13.8 h, respectively. The maximum elevation angle was about 37 degrees, and the energy threshold was estimated to be  $\sim 2$  TeV. The measured gamma ray fluxes within the energy range of 2 – 10 TeV are shown in Table 2 and Fig. 4. Figure 4 also shows power-law spectra obtained by H.E.S.S. and MAGIC [23, 24]. Using the measured fluxes, a fit for a power-law spectrum gives a differential flux normalization at 1 TeV of  $(2.9 \pm 2.8_{\text{stat}}) \times 10^{-11} \text{ cm}^{-2} \text{ sec}^{-1} \text{ TeV}^{-1}$  and a power-law index of  $2.57 \pm 0.59_{\text{stat}}$ . Although the obtained spectrum has relatively large statistical errors, the differential flux of CANGAROO-II at 4.6 TeV with a power-law spectrum showed good agreement with that of H.E.S.S., within 9% and MAGIC, within 14% [23, 24].

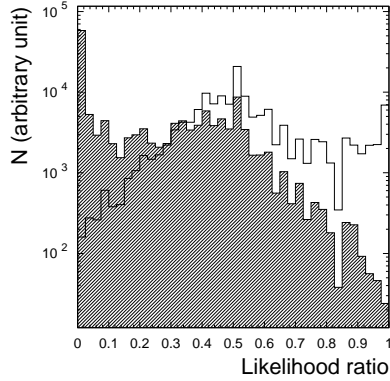


Figure 3: Distributions of Likelihood ratio ( $L_{\text{ratio}}$ ) for the gamma ray MC data (blank area) and OFF-source experimental data (hatched area). The number of the MC events are normalized to the OFF-source data. In this paper, we used the data with  $L_{\text{ratio}} > 0.4$ .

Table 2: Differential fluxes of the Crab nebula. Only statistical errors are estimated in this analysis.

Mean energy (TeV)	Differential flux (photons $\text{cm}^{-2} \text{sec}^{-1}$ )
$2.2 \pm 0.2$	$(3.7 \pm 3.0) \times 10^{-12}$
$2.9 \pm 0.3$	$(1.8 \pm 1.1) \times 10^{-12}$
$4.6 \pm 0.4$	$(6.3 \pm 2.9) \times 10^{-13}$
$8.6 \pm 0.5$	$(1.1 \pm 0.6) \times 10^{-13}$

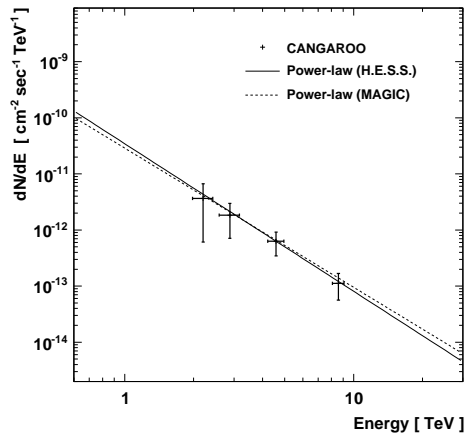


Figure 4: Differential fluxes of Crab and spectra from H.E.S.S. and MAGIC. Only statistical errors are shown.

## 4. Results

The left panel of Fig. 5 shows the energy dependence of the effective area for gamma rays of the region “p1” obtained by the MC simulation. The effective area is almost constant at

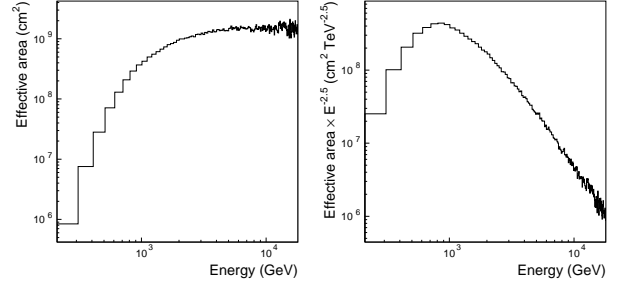


Figure 5: The effective area for gamma rays of the region “p1” is shown in left panel. The right panel shows the effective area multiplied by  $E^{-2.5}$ .

$\sim 1.5 \times 10^9 \text{ cm}^2$  above 2 TeV. The right panel of Fig. 5 shows the energy dependence of the detection efficiency for gamma rays of “p1”. Thus the energy threshold for gamma rays of “p1” is estimated to be 850 GeV from this distribution. The effective areas and the energy thresholds for “p2” and “p3” are estimated to be the same as for “p1”.

Figure 6 shows the distributions of the image orientation angle,  $Alpha$ , at “p1”, “p2” and “p3” for the combined data of 2001 and 2002. The number of OFF source events were normalized to the ON source data in the range of  $Alpha > 30$  degrees. The normalization factor was  $\sim 1.1$  for all regions. The number of excess events was obtained by subtracting the number of the OFF source events from the ON source events in the range of  $Alpha < 20$  degrees.

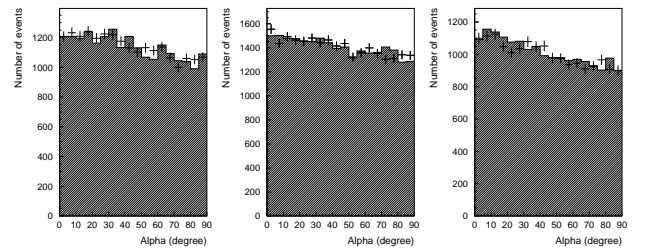


Figure 6:  $Alpha$  distributions of the combined data for “p1” (left), “p2” (middle) and “p3” (right). The points with statistical error bars show ON source data and hatched histograms show OFF source data.

The statistical significances of the excesses at “p1”, “p2” and “p3” were 0.39,  $-0.11$  and  $-1.0 \sigma$ , respectively. Since we found no significant excess from the data, we derived the 99% confidence level upper limit fluxes, using Helene’s method [25], to be  $1.5 \times 10^{-12}$ ,  $1.3 \times 10^{-12}$  and  $7.9 \times 10^{-13} \text{ cm}^{-2} \text{ sec}^{-1}$ , respectively, for VHE gamma rays with  $E > 850 \text{ GeV}$ . These results are summarized in Table 3.

Table 3: Results of a search for VHE gamma rays with the CANGAROO-II telescope from the western X-ray lobe observed by ASCA. The 99% C.L. upper limit fluxes are given above the energy threshold ( $E_{\text{th}} = 850$  GeV).

Source	R.A.	Decl.	<sup>a</sup> $N_s$	<sup>b</sup> $S$	<sup>c</sup> $\phi^{99\%}$
<i>p1</i>	19 <sup>h</sup> 10 <sup>m</sup> 17 <sup>s</sup>	+4°57′46″	39	0.39	1.5
<i>p2</i>	19 <sup>h</sup> 09 <sup>m</sup> 44 <sup>s</sup>	+4°58′48″	-12	-0.11	1.3
<i>p3</i>	19 <sup>h</sup> 09 <sup>m</sup> 12 <sup>s</sup>	+4°59′13″	-97	-1.0	0.79

<sup>a</sup> Number of Excess events included in  $Alpha < 20^\circ$ .

<sup>b</sup> Statistical significance in units of standard deviation  $\sigma$  [26].

<sup>c</sup> 99% C.L. upper limit flux for  $E \geq E_{\text{th}}$  in unit of  $10^{-12}$  ph cm<sup>-2</sup> s<sup>-1</sup>.

## 5. Discussion

According to the ASCA measurements, the X-ray lobes are considered to be generated by non-thermal emissions [12, 13]. The CANGAROO-II observations were carried out based on this ASCA result, aiming to detect the VHE gamma rays, but no evidence was found for gamma ray emissions above 850 GeV. We obtained upper limit fluxes which are useful to constrain the parameters of the western X-ray lobe based on the non-thermal model through a synchrotron/inverse-Compton (IC) emission process. Therefore, we try to understand the wide energy range of photon spectrum from radio to TeV using the synchrotron/IC model.

From ASCA X-ray data [12, 13], we extracted five data points in the energy region from 0.7 to 10 keV by fitting to the power-law spectrum. Similarly, we used the radio data of Downes et al. at 1.7, 2.7 and 4.75 GHz [1, 2]. The radio and X-ray fluxes of “*p1*”, “*p2*” and “*p3*” were calculated from the intensities of respective energy ranges correcting the FOV to the 8’ of ASCA.

As the seed photons for the IC process, we examined the possibility of IR radiation in addition to the cosmic microwave background (CMB). First, we checked the IR photon field. An upper limit to the IR flux is given by Band (1987) [27] for the optical filament region observed across “*p2*”. Using the upper limit flux, we have obtained the upper limits of respective energy densities as  $\sim 0.033$  eV cm<sup>-3</sup> at 12  $\mu$ m and  $\sim 0.047$  eV cm<sup>-3</sup> at 100  $\mu$ m. Since we have no information on IR flux at “*p1*” and “*p3*”, we assume the same upper limits for them. The upper limit values for the interval wavelengths are interpolated assuming a power-law spectrum.

Next, we checked optical photon field. Hillwig et al. (2004) [9] claimed that the normal star in the SS433 system was a type A3-7 I supergiant with a mass of  $10.9 \pm 3.1 M_\odot$ . This implies a typical temperature and stellar radius of  $T_s \sim 8000$  K and  $R_s \sim 40 R_\odot$  [28]. Assuming the normal star to be a blackbody radiator, we estimated the energy density to be  $\sim 0.067$  eV cm<sup>-3</sup> at the peak frequency of  $5.0 \times 10^{14}$  Hz. This value of energy density negligibly contributes to the IC process compared to the CMB. Further more, we evaluated the energy density of the optical filament, since “*p2*” includes the optical filament in the western lobe. From Boumis et al. (2007) [29], we obtained a energy density of  $\sim 10^{-4}$  eV cm<sup>-3</sup> for H $\alpha$  line, and the same energy density levels for other emission lines. Also from Mazej et al. (1983) [30], we obtained  $\sim 10^{-3}$  eV cm<sup>-3</sup> in N II

6584 Å line. Comparing these energy densities to that of CMB ( $\sim 0.26$  eV cm<sup>-3</sup>) coupled with the Klein–Nishina effects, the optical photon field provides almost negligible contribution to the IC process. Therefore, for all regions we do not take into account the optical photon field as the seed photons of IC emission. We also checked the possibilities that both the X-ray and radio photons of the western X-ray lobe can contribute as IC seed photons, and found negligibly small contributions compared to the CMB.

For the spectrum of electrons which drive the synchrotron/IC process, we assumed  $E^{-\gamma} \exp(-E/E_{\text{max}})$  where  $\gamma$  is the power-law index, and  $E_{\text{max}}$  is the exponential cutoff energy of electrons. Recent measurements of H I absorption/emission spectra and <sup>12</sup>CO spectrum toward SS433 support  $5.5 \pm 0.2$  kpc for the distance towards the SS433/W50 system, and constrain the age of W50 to be younger than  $10^5$  yr [31]. We obtained the expected fluxes for the synchrotron/IC model adopting a distance of  $D = 5.5$  kpc. The ratio between the size of synchrotron emission region and that of IC was assumed to be unity. We obtained moderately good fits for “*p2*” and “*p3*” on the interpretation for the wide energy range of the photon spectrum by freeing all four parameters. The fit for “*p2*” gives the lower limit of the strength on the magnetic field,  $B_{\text{min}}$ , to be  $4.3 \mu$ G with  $\chi^2 = 7.0/5$ , and the fit for “*p3*” gives  $B_{\text{min}} = 6.3 \mu$ G with  $\chi^2 = 15/5$ . The photon indices of both regions were estimated to be  $\sim 1.7$ . For “*p1*”, on the other hand, it is very difficult to understand the wide energy range of photon spectrum with a single synchrotron/IC emission model since the X-ray emission has a very hard spectrum. Hence, we presented the result under the assumption of a cutoff energy of electrons at “*p1*” as 510 TeV given by  $\sim 280$  TeV  $(E_X/1 \text{ keV})^{1/2} (B/1 \mu\text{G})^{-1/2}$  ( $E_X$ ; the energy of X-rays generated by the synchrotron process), using the X-ray energy of 10 keV and the strength on the magnetic field of  $3 \mu$ G. The obtained spectral energy distributions for “*p1*”, “*p2*” and “*p3*” are shown in Fig. 7.

The fit for “*p1*” giving  $\chi^2/dof = 420/7$  clearly indicates that a unified interpretation for the wide wavelengths from radio to TeV does not work well at “*p1*”. This result leads to an alternative interpretation that the X-ray emissions does not share the same radiation mechanism with the radio emissions. According to the ASCA result, the radial distribution of the hard X-rays (3.0 – 10.0 keV) shows a steep peak of  $\sim 3'$  spread at near the center of “*p1*” [12]. In contrast to such a “hot spot” feature, the radial distribution of the soft X-rays (0.7 – 3.0 keV) does not show a clear peak in “*p1*”, and is similar to that at “*p2*” and “*p3*” in both energy bands. Thus, the “*p1*” emission region is likely to be a combination of the spot-like hard X-ray emission at the center of “*p1*” together with diffuse X-rays similar to “*p2*” or “*p3*”. A similar morphological feature has been found by the recent X-ray measurement with *XMM-Newton* for the eastern X-ray lobe [32]. Based on this combined emission model for “*p1*”, it can be suggested that the diffuse emission region shares the radiation mechanism from the radio to X-ray energy and the hard X-ray spectrum is mainly dominated by the spot-like emissions. Therefore, we examined the synchrotron/IC emission model without the radio data, since the diffuse emissions are preferable to provide minor contribu-

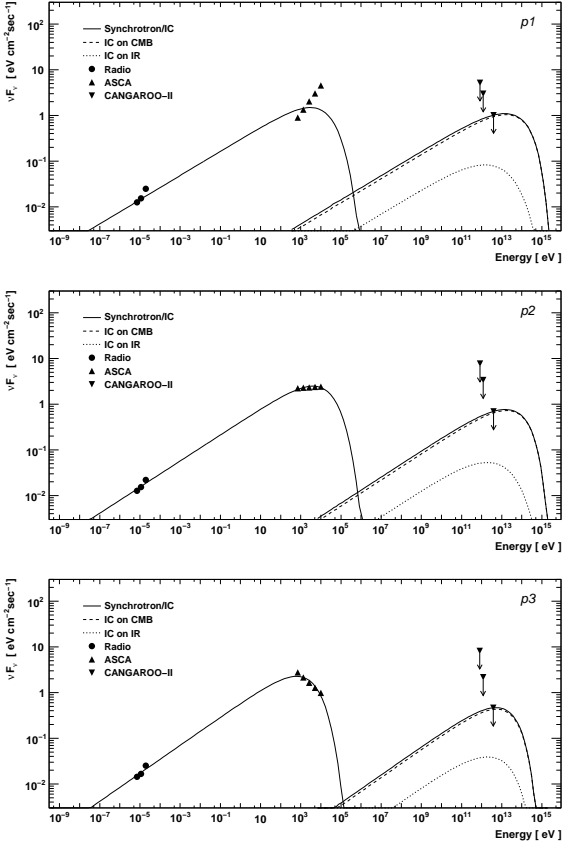


Figure 7: Synchrotron/IC model fitting to the spectral energy distributions at “p1” (top), “p2” (middle) and “p3” (bottom). The X-ray fluxes are from ASCA [12, 13] and the radio fluxes are calculated from the result of the Effelsberg 100-m telescope for each frequency [1, 4]. The 99% C.L. upper limit fluxes of this work are shown by down-arrows. Their mean energies are 0.9, 1.2 and 3.9 TeV, respectively. The thick solid lines represent the synchrotron/IC spectra. Two components (CMB and IR) of IC are shown by the dashed lines and the dotted lines, respectively.

tion for the X-ray spectrum. The alternative spectral energy distribution for “p1” is obtained as Fig. 8, assuming the same cutoff energy of  $E_{\max} = 510$  TeV and  $B = 3 \mu\text{G}$  as in Fig. 7. The resulting parameters for “p1”, “p2” and “p3” are summarized in Table. 4. As shown in Fig. 8, the expected flux of IC emissions at TeV region does not exceed our upper limit flux, hence it is found that the interpretation by this model is acceptable. Although this model is a possible case, it seems to require the combination of multiple emission components to understand the wide energy range of photon spectrum using the synchrotron/IC model for “p1”.

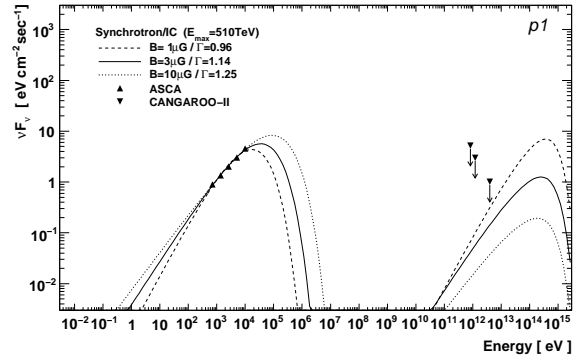


Figure 8: Alternative spectral energy distributions for “p1”. The data shown here are the same data with Fig. 7, although only the X-ray data are taken into account for this fit. The cutoff energy of electrons is set as same value of  $E_{\max} = 510$  TeV as Fig. 7. The solid line and the dotted line represent the synchrotron/IC spectra under the various magnetic field assumptions;  $B = 1, 3$  and  $10 \mu\text{G}$ , respectively.

Table 4: Fitted parameters for synchrotron/inverse-Compton model

Region	<sup>a</sup> $B_{\min}$ ( $\mu\text{G}$ )	$E_{\max}$ (TeV)	<sup>b</sup> $\Gamma$	$\chi^2/dof$
<sup>c</sup> p1	<sup>d</sup> 3.0	<sup>d</sup> 510	$1.1 \pm 0.0$	3.5/(5-2)
p2	$4.3 \pm 0.1$	$440 \pm 60$	$1.7 \pm 0.0$	7.0/(9-4)
p3	$6.3 \pm 0.3$	$130 \pm 10$	$1.7 \pm 0.0$	15/(9-4)

<sup>a</sup> Lower limit on the strength of the magnetic field.

<sup>b</sup> Photon index ( $= (\gamma + 1) / 2$ ).

<sup>c</sup> Result of a fit without the radio data.

<sup>d</sup> Assumed parameters.

## 6. Conclusion

According to the analysis of the ASCA data [12, 13] for SS433/W50 system, the X-ray spectra of 3 regions in the western part of the X-ray lobe can be explained by non-thermal emission. Therefore, shock acceleration may be present in this region and the emission of the VHE gamma rays may result.

Using the 10 m CANGAROO-II telescope, we have searched for gamma rays in the VHE region from the western part of the X-ray lobe of SS433/W50 system. We detected no significant excess of gamma rays from this region. To check the reliability of our observations and the analysis procedure, we analyzed

Crab nebula data using the same analysis code, and obtained consistent results with recent measurements by H.E.S.S. and MAGIC. The 99% confidence level upper limits on the fluxes of gamma rays for “*p1*”, “*p2*” and “*p3*” were as  $1.5 \times 10^{-12}$ ,  $1.3 \times 10^{-12}$  and  $7.9 \times 10^{-13} \text{ cm}^{-2} \text{ sec}^{-1}$  above 850 GeV, respectively. Using these upper limit fluxes, we derived the lower limits of the magnetic field as to be 4.3 and 6.3  $\mu\text{G}$  for “*p2*” and “*p3*”, respectively, under the assumption of a synchrotron/inverse-Compton model for the wide energy range of photon spectrum from radio to TeV. The same interpretation for “*p1*” was attempted and found to be difficult. However, we suggested the alternative interpretation for “*p1*” by assuming the combined X-ray emissions which consists of the diffused X-ray emissions and the spot-like hard X-ray emissions. Since the spot-like emissions were supposed to provide major contribution to the hard X-ray spectrum, we examined the model without the radio data and found this interpretation was acceptable.

The authors would like to thank Dr. N. Kawai and Dr. M. Namiki for providing us the ASCA X-ray data and helpful comments. This work was supported by a Grant-in-Aid for Scientific Research by the Japan Ministry of Education, Culture, Sports, Science and Technology (MEXT) of Japan, the 21st Century COE “Center for Diversity and Universality in Physics” from MEXT, the Australian Research Council, ARC Linkage Infrastructure Grant LE0238884, Discovery Project Grant DP0345983, JSPS Research Fellowships, and the Promotion and Mutual Aid Corporation for Private Schools of Japan. We thank the Defense Support Center Woomera and BAE Systems.

## References

- [1] A. J. B. Downes, T. Pauls, C. J. Salter, MNRAS 218 (1986) 393–407.
- [2] A. J. B. Downes, C. J. Salter, T. Pauls, A&A 103 (1981) 277–287.
- [3] R. Elston, S. Baum, AJ 94 (6) (1987) 1633–1640.
- [4] B. J. Geldzahler, T. Pauls, C. J. Salter, A&A 84 (1980) 237–244.
- [5] R. M. Hjellming, K. J. Johnston, ApJ 246 (1981) L141–L145.
- [6] R. C. Vermeulen, et al., A&A 270 (1993) 177–188.
- [7] B. Margon, et al., ApJ 230 (1979) L41–L45.
- [8] B. Margon, S. F. Anderson, ApJ 347 (1989) 448–454.
- [9] T. C. Hillwig, et al., ApJ 615 (2004) 422–431.
- [10] M. G. Watson, et al., ApJ 273 (1983) 688–696.
- [11] S. Safi-Harb, H. Ögelman, ApJ 483 (1997) 868–881.
- [12] M. Namiki, et al., Adv. Space Res. 25 (2000) 709–712.
- [13] M. Namiki, T. Kawai, T. Kotani, Private communication, 2000.
- [14] F. Aharonian, et al., A&A 439 (2005) 635–643.
- [15] M. Mori, et al., in: Proc. 27th Internat. Cosmic Ray Conf. (Hamburg), vol. 5, 2831–2834, 2001.
- [16] A. Kawachi, et al., Astropart. Phys. 14 (2001) 261–269.
- [17] R. Enomoto, et al., Nature 416 (2002) 823–826.
- [18] A. M. Hillas, in: Proc. 19th Internat. Cosmic Ray Conf., vol. 3, 445–448, 1985.
- [19] T. C. Weekes, et al., ApJ 342 (1989) 379–395.
- [20] A. V. Plyasheshnikov, G. F. Bignami, Nuovo Cimento 8C (1985) 39–54.
- [21] M. Punch, et al., Nature 358 (1992) 477–478.
- [22] R. Enomoto, et al., Astropart. Phys. 16 (2002) 235–244.
- [23] F. Aharonian, et al., A&A 457 (2006) 899–915.
- [24] J. Albert, et al., ApJ 674 (2008) 1037–1055.
- [25] O. Helene, Nuclear Instruments and Methods in Physics Research 212 (1983) 319–322.
- [26] T. P. Li, Y. Q. Ma, ApJ 272 (1983) 317–324.
- [27] D. L. Band, PASP 99 (1987) 1269–1276.
- [28] K. A. Venn, ApJS 99 (1995) 659–692.
- [29] P. Boumis, et al., MNRAS 381 (2007) 308–318.
- [30] T. Mazeh, et al., ApJ 265 (1983) 235–238.
- [31] F. J. Lockman, K. M. Blundell, W. M. Goss, MNRAS 381 (2007) 881–893.
- [32] W. Brinkmann, et al., A&A 463 (2007) 611–619.